Journal of Electronic Materials (2023) 52:917–924
https://doi.org/10.1007/s11664-022-10106-x

ORIGINAL RESEARCH ARTICLE

# Investigation of Single-Metal Fe-Based Metal–Organic Framework as an Electrocatalyst for a Rechargeable Zinc-Air Battery

**Upasana Bhardwaj[1] · Prachi Janjani[2] · Ravindra Sharma[1] · H. S. Kushwaha[1]**

Received: 8 August 2022 / Accepted: 15 November 2022 / Published online: 7 December 2022


## Abstract

With the advantage of high protection and energy density, the zinc-air battery (ZAB) has shown potential for practical applications in energy research. Metal–organic frameworks (MOFs) are being explored as bifunctional alternatives to replace precious metals. In this work, a new MIL-88B(Fe) MOF was developed and investigated for a rechargeable ZAB. The MOF catalyst was characterized to determine its structure, morphology, pure composition, and porosity. The oxygen reduction reaction (ORR) and oxygen evolution reaction (OER) performance was also examined in alkaline solutions with $O_2$ and $N_2$ purging, respectively. The zinc-air cell so developed exhibits good performance with a power density of 101 mW $cm^{-2}$ at 65 mA $cm^{-2}$ current density. The rechargeable Fe-MOF ZAB also shows high cyclic stability with minimum fluctuation at 5 mA $cm^{-2}$ for 500 cycles. The observed results prove that Fe-MOF is a promising catalyst for ZABs.

## Graphical Abstract

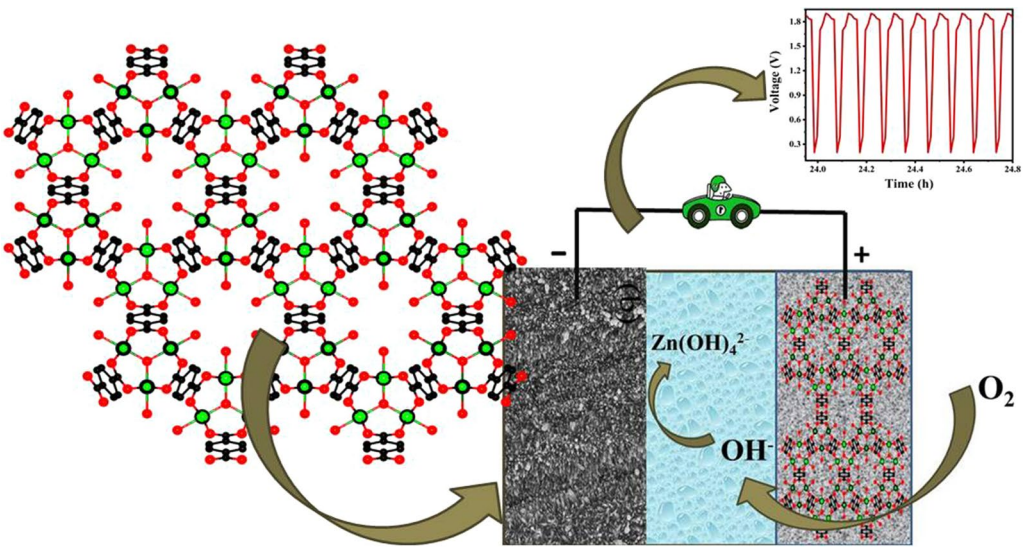


**Keywords** Metal organic frameworks · Fe-MOF · zinc air battery · ORR-OER

✉ H. S. Kushwaha
himmatsingh.mrc@mnit.ac.in

[1] Materials Research Centre, Malaviya National Institute of Technology Jaipur, Jaipur, Rajasthan 302017, India

[2] Department of Chemistry, School of Chemical Sciences and Pharmacy, Central University of Rajasthan, Ajmer 305817, India

## Introduction

In recent years, zinc-air technology has emerged as a promising option in energy research focused on creating efficient, cheap, and environmentally friendly models.[1] Zinc-air batteries (ZABs) show enhanced storage capability, with a

theoretical energy density of 1353 Wh/kg and volumetric energy density of 6136 Wh/L with an open-circuit voltage (OCV) of 1.65 V.[2–5] The battery component involves zinc electrodes, which are low-cost due to their abundance, low equivalent weight, environmental benignity, and safety.[6–10] ZABs also enable easy charging, minimum toxicity, no corrosion, and reduced possibility of thermal runaway.[11,12]

However, the poor catalytic activity of an air electrode during charge–discharge hinders its practical applications occurring in the slow oxygen reduction and evolution reactions (ORR-OER) in the process.[13] Noble precious-metal-based electrocatalysts such as platinum (Pt) for ORR and Ir-/Ru-$O_2$ for OER have been investigated as the most efficient catalysts for ZABs.[7,14–17] But the high cost and scarcity of these precious metals limit the industrial application of ZABs. Therefore, much research has been carried out recently to investigate and synthesize an efficient, low-cost bifunctional electrocatalyst for ZABs.[18] Much effort has been devoted to investigating non-precious efficient bifunctional catalysts. Many metal oxides and perovskites have been explored, including $MnO_2$, $Sr_2TiMnO_6$, $LaMnO_3$, and their composites, which are comparable to the precious metal option.[2,6,15] Despite the structural flexibility and enhanced oxygen reduction activity, they do not provide better performance. Hence, it is crucial to investigate and develop a non-precious electrocatalyst for ZAB applications.

Metal–organic frameworks (MOFs), which benefit from the arrangement of transition metals (e.g., Ni, Co, Fe) and organic ligands with heteroatoms (e.g., N, B, S), have recently received considerable attention as resources for the intentional design of effective and bifunctional non-precious metal catalysts for use in ZABs as air cathodes.[19] Metal–organic frameworks (MOFs) are materials that are porous and interconnected by ions or clusters (metal nodes) bound to organic ligands in repeating coordination units.[19,20] MOFs have controllable functionality, adsorption affinity, and a high surface area due to their hollow three-dimensional nanostructures, making them a viable option. Wenhen et al. proposed a mesoporous nitrogen-doped graphene sheet derived from amorphous MOFs. In this study, the developed ZAB attains a power density of 97.7 mW $cm^{-2}$ at a high current density of 120 mA $cm^{-2}$, proving MOFs to be a competent option for ZABs.[21]

In this work, an electrocatalyst Fe-MOF, derived from MIL-88B(Fe) structure, was developed and investigated for a ZAB. MIL-88B(Fe) is built from trimeric $Fe_3$-$\mu_3$-oxo clusters as secondary binding units (SBUs) interconnected to terephthalate linkers. The catalyst was characterized to determine its structure, morphology, pure composition, and porosity. The electrochemical activity of Fe-MOF was also tested to evaluate the ORR-OER activity using a rotating disk electrode (RDE) in alkaline media. The ZAB cell was also developed and assessed in ambient air conditions.

## Experimental

### MIL-88(Fe) MOF Synthesis

A previously reported solvothermal method was used to synthesize the MIL-88B(Fe) MOF.[22] Briefly, 10 mmol $Fe(NO_3).(H_2O)$ and 10 mmol of 1,4 benzene dicarboxylic acid ($H_2BDC$) were dissolved in 50 mL of *N*,*N*-dimethyl formamide (DMF) and agitated for 30 min. To this mixture, 4 mL of 2 M NaOH solution was added. The mixture was placed in a steel autoclave with Teflon lining for 12 h and maintained at 100°C. The solid was recovered by filtration and washed three times using ethanol and water. The collected solid was re-suspended in deionized water and stirred overnight to remove the residual solvent from the framework. Finally, MIL-88B(Fe) powder was obtained by vacuum drying the product for 8 h at 75°C.

### Characterization Tools

The crystallographic information of the as-synthesized MIL-88B(Fe) MOF was established using a PANalytical X'Pert PRO x-ray diffractometer employing a $CuK_\alpha$ source of 1.54 Å operating at 40 kV and 40 mA under a $2\theta$ step size of 0.02°. The surface morphology of the sample was obtained using a field-emission scanning electron microscope (Nova NanoSEM 450, FEI). The molecular structure of the MOF was investigated by employing attenuated total reflectance-Fourier transform infrared (ATR-FTIR) spectroscopy (Alpha, Bruker) in the wavenumber range of 4000–500 $cm^{-1}$. An x-ray photoelectron spectroscope (Omicron ESCA Probe, Omicron Nanotechnology) equipped with a monochromatic $AlK_\alpha$ source ($h\nu = 1486.7$ eV) was used to evaluate the chemical composition of the synthesized MOF. The $N_2$ adsorption–desorption isotherm of the sample was obtained on a Quantachrome NOVATouch LX2 gas sorption analyzer.

### Electrochemical Tests

The electrochemical tests were conducted on a BioLogic SP-150 three-electrode electrochemical workstation, with glassy carbon (RDE, 3 mm) as a working electrode and Ag/AgCl and platinum wire as reference and counter electrodes, respectively. The experiment was performed in 0.1 M and 1 M KOH with $N_2$ and $O_2$ purging. The catalytic ink for the test was prepared by mixing 5 mg Fe-MOF and 1 mg Vulcan carbon XC-72 with 10 uL of 5 wt.% Nafion solution, dispersed in 100 uL of isopropyl alcohol (IPA) solution until a homogeneous solution was obtained. Ten

microliters of the ink was loaded on the RDE electrode for electrochemical analysis.

### Design and Fabrication of the Battery

A rechargeable battery was designed using the bifunctional catalyst Fe-MOF-coated nickel-foam of 1.2 $cm^2$. Zinc foil was used as an anode with 6 M and 0.2 M KOH and zinc acetate $Zn(Ac)_2$, respectively. The catalyst ink was prepared by mixing Fe-MOF and carbon black in a ratio of 1:1. A solution of 30 µL Nafion was added as a binder and dispersed in 1 mL of IPA solution. Next, 100 µL of the ink was applied to the electrode and dried for 5 h at 60°C in a vacuum oven. The zinc-air cell was tested on a battery cycler (Neware battery testing system).

## Results and Discussion

### Material Characterization

XRD patterns were recorded to obtain the crystal phase purity of MIL-88B(Fe). As shown in Fig. 1a, the peaks occurring at $2\theta = 8.79°$, 10.27°, 17.51°, 25.27°, 28.07°, 33.27°, and 35.71° were well matched with the pattern simulated from the MIL-88(Fe) crystallographic information file (CCDC No. 1485530), which crystallizes in the $P6_3/mmc$ space group.[23]

The vibrational bands of the MIL-88B(Fe) MOF were analyzed using its FT-IR spectrum, as shown in Fig. 1b. Fe–O bond stretching was responsible for the sharp peak at 526 $cm^{-1}$. The peak at 623 $cm^{-1}$ was also attributed to the $Fe_3$-O metal-oxo cluster of the MIL-88B(Fe) structure.[24] A broad peak at 3200–3000 $cm^{-1}$ was responsible for the O–H stretching vibration. Peaks at 1598 $cm^{-1}$ and 1382 $cm^{-1}$were attributed to asymmetric and symmetric vibrations of carboxyl groups. The peaks at 1295 $cm^{-1}$ and 1019 $cm^{-1}$ were attributed to the C=C and C–C groups stretching the organic ligand. The peak at 746 $cm^{-1}$ contributed to the C–H bending vibrations of benzene.[25] The scanning electron micrographs of MIL-88B(Fe) shown in Fig. 1c depict a needle-shaped morphology of about 2.2 µm in length and 0.42 µm in diameter. On the other hand, the surface morphology of the synthesized MOF remained irregular in shape. Figure S1 (Supplementary file) shows homogeneity in the shape and size of the synthesized catalyst.

The binding states and chemical composition of the synthesized MIL-88B(Fe) MOF were investigated using x-ray photoelectron spectroscopy (XPS). Figure 2a shows peaks corresponding to three elements (O 1s, C 1s, and Fe 2p) observed in the XPS survey spectrum performed in the binding energy range of 0 eV to 900 eV. Figure 2b shows a significant spectrum of C 1s with three peaks, 284.09 eV,

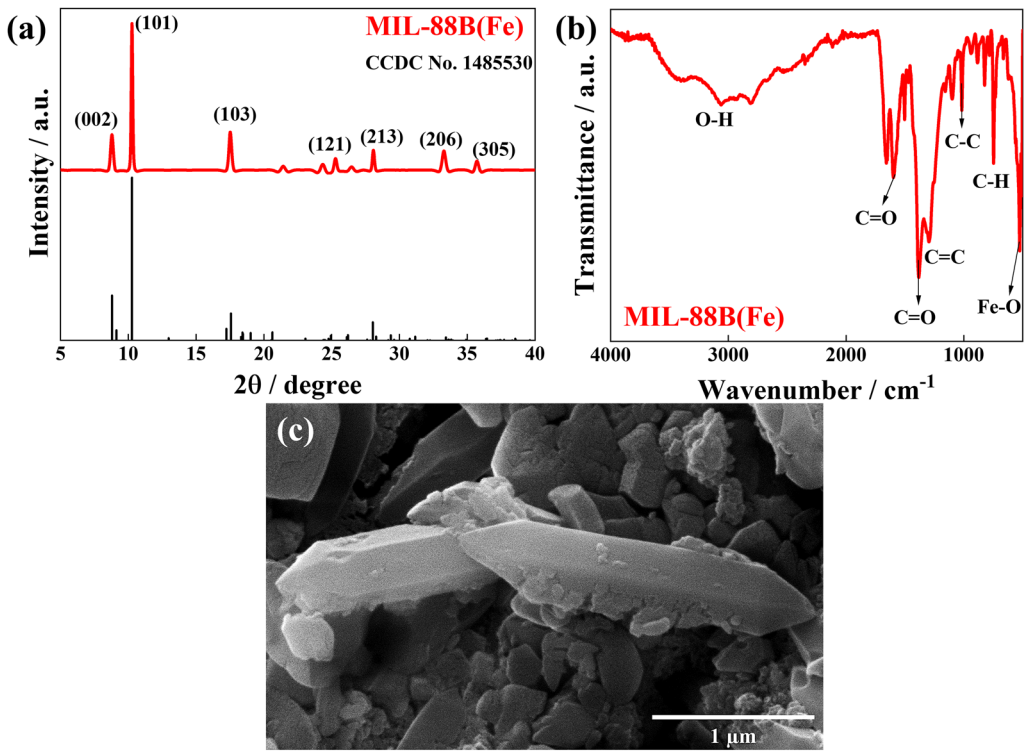


**Fig. 1** (a) XRD patterns of MIL-88B(Fe); (b) FTIR of Fe-MOF; (c) SEM images of the synthesized catalyst.

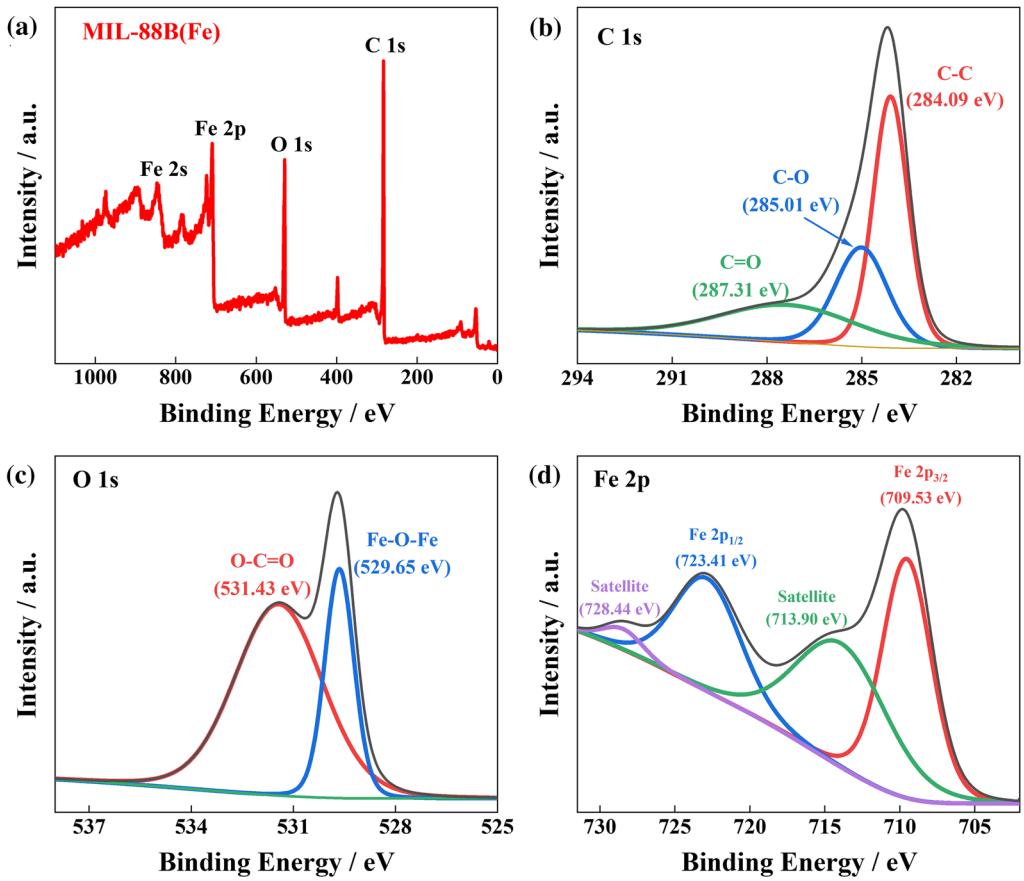


**Fig. 2** (a) XPS survey of the as-prepared MIL-88B(Fe) catalyst; (b–d) individual analysis of the FE-MOF.

285.01 eV, and 287.31 eV, attributed to the C–C/C=C, C–O, and C=O groups of the terephthalate linker in the framework, respectively.[26] The O 1s spectrum was deconvoluted into two peaks, as shown in Fig. 2c. The peak at 529.64 eV confirmed the Fe–O metal-oxo coordination linkages in the MIL-88B(Fe) framework. In contrast, the carboxylate linkages, such as conjugated O–C=O chemical bonds, were attributed to the peak at 531.43 eV.[27] The Fe 2p spectra were resolved into four peaks, as shown in Fig. 2d. The peaks at 709.53 eV and 723.41 eV were attributed to the Fe $2p_{3/2}$ and Fe $2p_{1/2,}$ with the peak separation being ~ 14 eV, which is attributed to the +3 oxidation state of Fe.[28,29] Additionally, satellite shakeups were observed at 713.90 and 728.44 eV, implying that all the iron content in the MOF is of the form $Fe^{3+}$ ions.[30]

The $N_2$ adsorption–desorption isotherm and multipoint plot of MIL-88B(Fe) MOF are shown in Fig. 3a and b. For MIL-88B(Fe), a type IV sorption isotherm with H3 hysteresis was observed, resulting in slit-like pores.[31] The sample presented a mesoporous structure, with a pore size of 1 to 80 nm, as shown in Fig. 3c. Using Brunauer–Emmett–Teller (BET) theory, the specific surface area was calculated to be 5.82 $m^2g^{-1}$. The mean pore diameter was 1.70 nm, and the pore volume was found to be 0.015 $cm^3\ g^{-1}$.

## Electrochemical Results

Battery performance is crucially affected by sluggish oxygen reactions: ORR (oxygen reduction reaction) and OER (oxygen evolution reaction). Figure 4a shows the reaction mechanism of ORR-OER. To evaluate the overpotential factor of the catalyst, bifunctional ORR/OER cyclic voltammetry was conducted in 0.1 M $N_2$ purged KOH within a potential range of 0 to 2.2 V versus reversible hydrogen electrode (RHE) and at a scan rate of 20 mV/s, as shown in Fig. 4b. LSV was taken in the potential window of 1.0 V to 2.2 V versus RHE to analyze the oxygen evolution activity, as shown in Fig. 4c. The overpotential was calculated to be 0.7 V (1.99–1.23 V) at a current density of 10 mA $cm^{-2}$. The Tafel value was obtained to be 178 mV $dec^{-1}$ using the Tafel equation: $\eta = \text{blog}J$, as shown in Fig. 4d.

Metal-air batteries work on either two-electron or four-electron pathways. The four-electron pathway is preferred because no peroxide is formed as a byproduct. Hence, to determine the electron pathways followed by the catalyst,

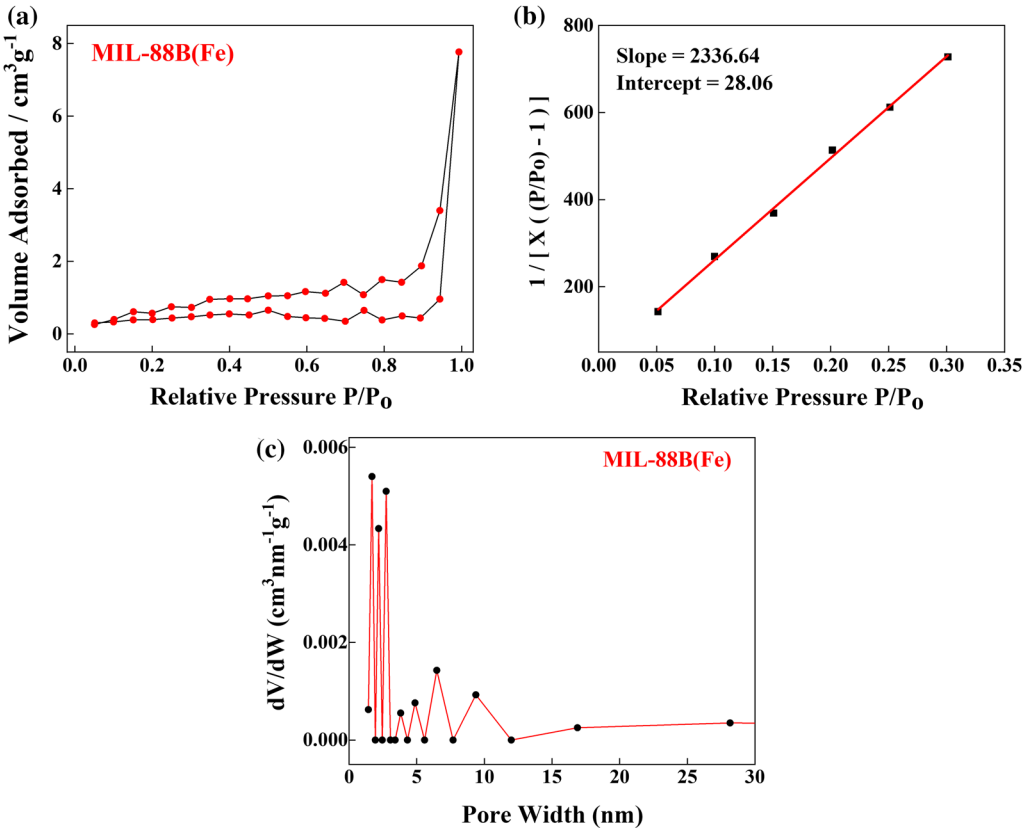


**Fig. 3** (a) $N_2$ desorption and adsorption isotherms; (b) BET multipoint graph for MIL-88B(Fe); (c) pore size distributions of the Fe-MOF sample.

an ORR test was performed on a three-electrode system (Ag/AgCl as a reference electrode, Pt wire as counter electrode, and rotating glassy carbon as a working electrode) in 0.1 M KOH with $O_2$ purging. Figure 5a shows linear sweep voltammetry (LSV) at varying rotation rates from 0 rpm to 3600 rpm in a voltage window of 1.0 to 0 V versus RHE. The onset potential ($E_0$) of the Fe-MOF was obtained to be 0.84 V, and the half-wave potential ($E_{1/2}$) is 0.8 V. Figure 5b displays the Tafel plot for the ORR, which shows a calculated Tafel value of 340 mV/dec. Further, to demonstrate the ORR electron pathway, a K-L plot was drawn between $1/\sqrt{w}$ versus $J^{-1}$ (mA $cm^{-2})^{-1}$, as shown in Fig. 5c. With the linear nature and first-order kinetics, the actual number of electrons transferred was 3.7 at 0.45 V. A bifunctional ORR/OER LSV comparison curve is shown in Fig. 5d in a potential range of 0 to +2 V versus RHE. The ΔE (electrode voltage difference) was derived by

$$\Delta E = E_{j=10\,OER} - E_{1/2\,ORR}$$

The potential difference (ΔE) was calculated to be 1.19 V at 5 mA $cm^{-2}$ with $Ej_{=10\ OER} = 1.99$ V and $E_{1/2\ ORR} = 0.8$ V, respectively.

## Zinc-Air Battery Test and Results

An aqueous battery was developed using an as-prepared cell setup of an air electrode as a cathode, alkaline electrolyte (KOH: 6 M + 0.2 M Zn $(Ac)_2$), and zinc anode. The battery shows an open-circuit voltage (OCV) of 1.1 V. Figure 6a depicts a galvanodynamic test of current density versus voltage polarization at current densities ranging between 0 mA $cm^{-2}$ and 120 mA $cm^{-2}$. The power density obtained was 101 mW $cm^{-2}$ at 65 mA $cm^{-2}$ current density. To test the energy storage capability of the as-prepared zinc-air cell, a galvanodynamic constant discharge test was conducted for 12 h, as shown in Fig. 6b. The battery demonstrates a continuous discharge voltage of 0.19 V with a specific capacity of 575 mA h $g^{-1}$. A galvanodynamic charge–discharge test was performed for

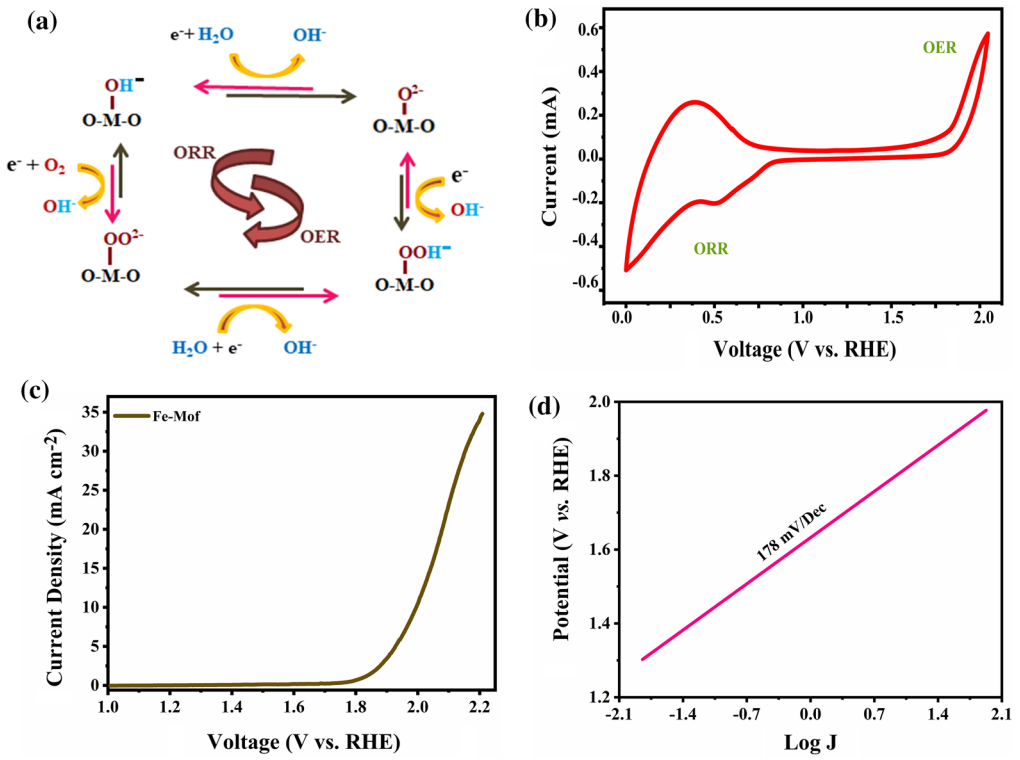


**Fig. 4** (a) ORR-OER reaction mechanism. Electrochemical evaluation of MIL-88B(Fe) for OER in 0.1 M KOH, $N_2$ purging. (b) Bifunctional ORR/OER cyclic voltammogram at a scan rate of 20 mV/s; (c) LSV plots at different rpm; (d) Tafel plot for the MOF sample.

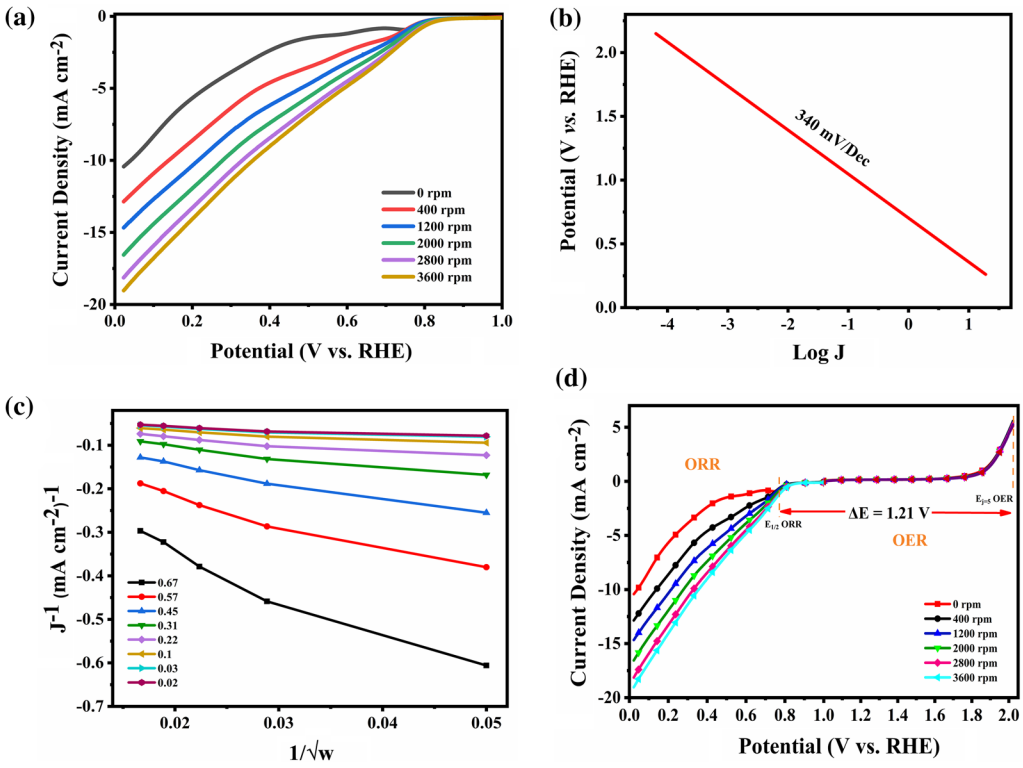


**Fig. 5** Electrochemical evaluation of MIL-88B(Fe) for ORR in 0.1 M KOH, $O_2$ purging. (a) LSV plots at different rpm; (b) Tafel plot for the Fe-Mof sample; (c) K-L plot at different potential; (d) bifunctional ORR/OER LSV curves.

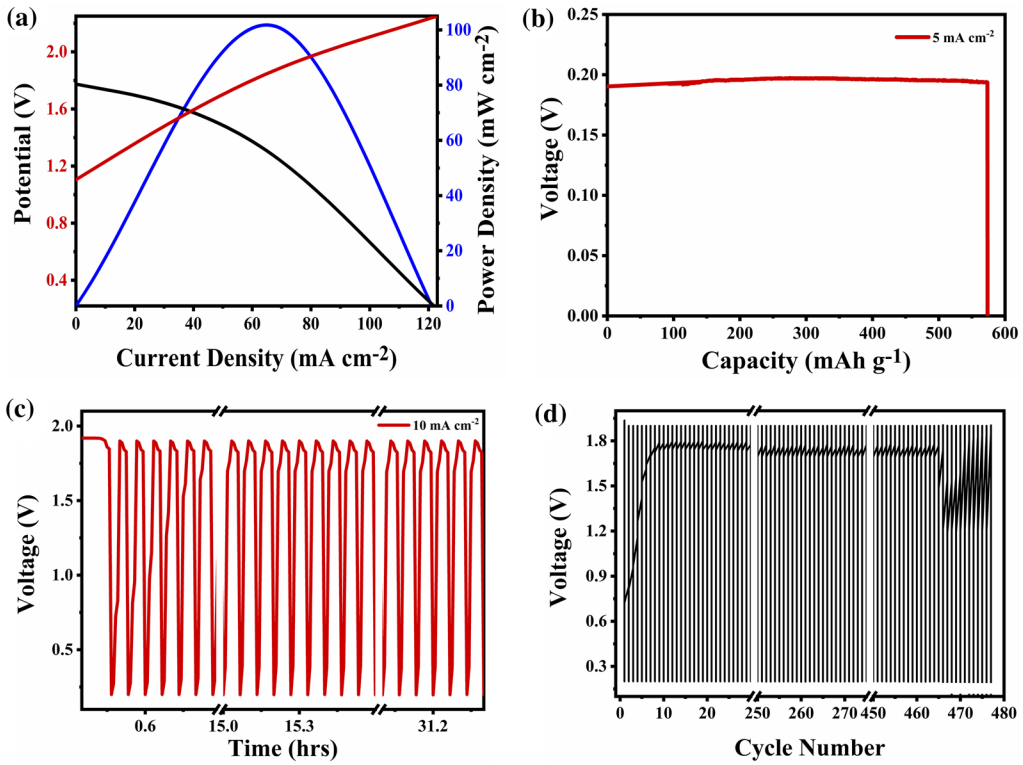


**Fig. 6** Performance of the developed ZAB. (a) Polarization curve with power density; (b) discharge curve at a current density of 5 mA $cm^{-2}$; (c) charge–discharge curves with the overpotential detail in the inset; (d) battery voltage versus cycle number.

500 cycles for several hours to check the battery's stability and cyclability. Figure 6c clearly shows that the battery performance was stable for 45 h in a potential range of 0.2–1.9 V. The potential gap achieved was 1.7 V at a fixed current density of 5 mA $cm^{-2}$. Figure 6d shows the cycle number versus potential (V), indicating the battery's overall performance. The result shows good stability with minimum to no fluctuations.

## Conclusion

In summary, Fe-MOF was synthesized using a solvothermal method to evaluate the performance of ZABs. The Tafel value was obtained to be 178 mV $dec^{-1}$, and the ΔE was calculated to be 1.19 V, indicating the potential difference in the ORR-OER activity of ZAB. The developed battery was tested under alkaline conditions in an ambient environment. The specific capacity calculated was 575 mA h $g^{-1}$ at a current density of 5 mA $cm^{-2}$. The power density was also estimated to be 101 mW $cm^{-2}$. The zinc-air cell exhibits excellent cyclic stability for 500 charge–discharge cycles. Hence, Fe-MOF can be regarded as an effective catalyst for a ZAB.

**Supplementary Information** The online version contains supplementary material available at https://doi.org/10.1007/s11664-022-10106-x.

**Acknowledgments** The authors are grateful to the WTI and DST for providing funding under the Water Technology Initiative Programme Project No. (EWFH/2019/222) and the DST-Inspire faculty scheme.

**Conflict of interest** On behalf of all authors, the corresponding author states that there is no conflict of interest.

## References

1. Q. Li, W. Xiong, S. Yu, Y. Liu, J. Li, L. Liu, X. Bi, G. Zhu, E. Liu, Y. Zhao, and B. Wang, Effect of Gd content on the discharge and electrochemical behaviors of the magnesium alloy AZ31 as an anode for Mg-air battery. *J. Mater. Sci.* 56, 12789 (2021).
2. U. Bhardwaj, A. Sharma, A. Mathur, A. Halder, and H.S. Kushwaha, Synthesis of a novel $Sr_2TiMnO_6$ double perovskite electrocatalyst for rechargeable zinc–air batteries. *Energy Storage.* 1, 109 (2021).
3. H. Lee, O. Gwon, C. Lim, J. Kim, O. Galindev, and G. Kim, Advanced electrochemical properties of $PrBa_{0.5}Sr_{0.5}Co_{1.9}Ni_{0.1}O_{5+\delta}$ as a bifunctional catalyst for rechargeable zinc-air batteries. *Chem. Electro. Chem.* 6, 3154 (2019).
4. J. Meng, F. Liu, Z. Yan, F. Cheng, F. Li, and J, Spent alkaline battery-derived manganese oxides as efficient oxygen electrocatalysts for Zn-air batteries. *Chen. Inorg. Chem. Front.* 5, 2167 (2018).

5. O. Krichevski, R.K. Singh, E. Bormashenko, Y. Bormashenko, V. Multanen, and A. Schechter, Bioinspired oxygen selective membrane for Zn-air batteries. *J. Mater. Sci.* 56, 9382 (2021).
6. U. Bhardwaj, A. Sharma, A. Mathur, A. Halder, and H.S. Kushwaha, Novel guar- gum electrolyte to aggrandize the performance of $LaMnO_3$ perovskite- based zinc-air batteries. *Electrochem. Sci. Adv.* 1, 105 (2021).
7. Y. Wang, J. Fu, Y. Zhang, M. Li, F.M. Hassan, G. Li, and Z. Chen, Continuous fabrication of a MnS/Co nanofibrous air electrode for wide integration of rechargeable zinc-air batteries. *Nanoscale* 9, 15865 (2017).
8. H.F. Wang, C. Tang, B. Wang, B.Q. Li, X. Cui, and Q. Zhang, Defect-rich carbon fiber electrocatalysts with porous graphene skin for flexible solid-state zinc-air batteries. *Energy Storage Mater.* 15, 124 (2018).
9. X. Zhang, R. Liu, Y. Zang, G. Liu, S. Liu, G. Wang, Y. Zhang, H. Zhang, and H. Zhao, Shrimp-shell derived carbon nanodots as precursors to fabricate Fe, N-doped porous graphitic carbon electrocatalysts for efficient oxygen reduction in zinc-air batteries. *Inorg. Chem. Front.* 3, 910 (2016).
10. Y. Bu, O. Gwon, G. Nam, H. Jang, S. Kim, Q. Zhong, J. Cho, G. Kim, and J., A highly efficient and robust cation ordered Perovskite oxides as a Bi-functional catalyst for rechargeable zinc-air batteries. *ACS Nano.* 11, 11594 (2017).
11. T. Warang, N. Patel, R. Fernandes, N. Bazzanella, and A. Miotello, $Co_3O_4$ nanoparticles assembled coatings synthesized by different techniques for photo-degradation of methylene blue dye. *Appl. Catal. B Environ.* 132–133, 204 (2013).
12. A.R. Mainar, O. Leonet, M. Bengoechea, I. Boyano, I. De Meatza, A. Kvasha, A. Guerfi, and J.A. Blázquez, Alkaline aqueous electrolytes for secondary zinc-air batteries: An overview. *Int. J. Energy Res.* 40, 1032 (2016).
13. Q.R. Pan, S.J. Li, K. Tong, C. Xie, L. Peng, N. Li, D.Y. Wang, H.J. Su, and J., Engineering $Ni^{3+}$ inside nickel selenide as efficient bifunctional oxygen electrocatalysts for Zn-air batteries. *Mater. Sci.* 54, 9063 (2019).
14. L. Yan, Y. Xu, P. Chen, S. Zhang, H. Jiang, L. Yang, Y. Wang, L. Zhang, J. Shen, X. Zhao, and L. Wang, A Freestanding 3D heterostructure film stitched by MOF-derived carbon nanotube microsphere superstructure and reduced graphene oxide sheets: A superior multifunctional electrode for overall water splitting and Zn–air batteries. *Adv. Mater.* 32, 1 (2020).
15. U. Bhardwaj, High energy storage capabilities of $CaCu_3Ti_4O_{12}$ for paper-based zinc-air battery. *Sci. Rep.* 12, 1 (2021).
16. Z. Deng, Q. Yi, G. Li, Y. Chen, X. Yang, and H. Nie, NiCo-doped C-N nano- composites for cathodic catalysts of Zn-air batteries in neutral media. *Electrochim. Acta* 279, 1 (2018).
17. J. Hu, L. Wang, L. Shi, and H. Huang, Oxygen reduction reaction activity of $LaMn_{1-x}Co_xO_3$-graphene nanocomposite for zinc-air battery. *Electrochim. Acta* 161, 115 (2015).
18. S. Zhao, K. Wang, S. Tang, X. Liu, K. Peng, Y. Xiao, and Y. Chen, A new solid-state zinc-air battery for fast charge. *Energy Technol.* 8, 1 (2020).
19. X. Yang, X. Wu, Z. Guo, Q. Li, H. Wang, C. Ke, W. Zeng, X. Qiu, Y. He, X. Liang, and Y. Kim, Phosphorus/nitrogen co-doped and bimetallic MOF-derived cathode for all-solid-state rechargeable zinc-air batteries. *RSC Adv.* 10, 33327 (2020).
20. J.C. Li, X.T. Wu, L.J. Chen, N. Li, and Z.Q. Liu, Bifunctional MOF-derived Co-N- doped carbon electrocatalysts for high-performance zinc-air batteries and MFCs. *Energy* 156, 95 (2018).
21. W. Niu and Y. Yang, Amorphous MOF Introduced N-doped graphene: An efficient and versatile Electrocatalyst for zinc-air battery and water splitting. *ACS Appl. Energy Mater.* 1, 2440 (2018).
22. P. Horcajada, F. Salles, S. Wuttke, T. Devic, D. Heurtaux, G. Maurin, A. Vimont, M. Daturi, O. David, E. Magnier, N. Stock, Y. Filinchuk, D. Popov, C. Riekel, G. Férey, and C. Serre, How linker's modification controls swelling properties of highly flexible iron(III) dicarboxylates MIL-88. *J. Am. Chem. Soc.* 133, 17839 (2011).
23. S. Dawood, S. Shaji, G. Pathiraja, Y. Mo, and H. Rathnayake, Phys Molecular magnetism in nanodomains of isoreticular MIL-88(Fe)-MOFs. *Chem. Chem. Phys.* 23, 21677 (2021).
24. G.T. Vuong, M.H. Pham, and T.O. Do, Direct synthesis and mechanism of the formation of mixed metal $Fe_2Ni$-MIL-88B. *CrystEngComm* 15, 9694 (2013).
25. T.A. Vu, G.H. Le, H.T. Vu, K.T. Nguyen, T.T.T. Quan, Q.K. Nguyen, H.T.K. Tran, P.T. Dang, L.D. Vu, and G.D. Lee, Highly photocatalytic activity of novel Fe-MIL-88B/GO nanocomposite in the degradation of reactive dye from aqueous solution. *Mater. Res. Express* 4, 408 (2017).
26. H. Zhang, X. Gong, Z. Song, S. Zhang, W. Du, T.T. Nguyen, M. Guo, and X. Gao, Wood-based carbon quantum dots for enhanced photocatalysis of MIL-88B(Fe). *Opt. Mater.* 113, 110865 (2021).
27. T. Van Tran, V.H. Nguyen, L.X. Nong, H.T.T. Nguyen, D.T.C. Nguyen, T.T. Nguyen, H.T.T. Nguyen, and T.D. Nguyen, Hexagonal Fe-based MIL-88B nanocrystals with $NH_2$ functional groups accelerating oxytetracycline capture via hydrogen bonding. *Surf. Interf.* 20, 100605 (2020).
28. K. Pandi and J. Choi, Selective removal of anionic ions from aqueous environment using iron-based metal-organic frameworks and their mechanistic investigations. *J. Mol. Liq.* 329, 115367 (2021).
29. T. Yamashita and P. Hayes, Analysis of XPS spectra of $Fe^{2+}$ and $Fe^{3+}$ ions in oxide materials. *Appl. Surf. Sci.* 254, 2441 (2008).
30. P. Hu, C. Yao, L. Yang, Y. Xin, and Y. Miao, Boosted photodegradation of tetracycline hydrochloride over Z-scheme MIL-88B(Fe)/$Bi_2WO_6$ composites under visible light. *Coll. Surfa. A Physicochem. Eng. Asp.* 627, 127248 (2021).
31. S. Brunauer, P.H. Emmett, and E. Teller, Adsorption of Gases in Multimolecular Layers. *J. Am. Chem. Soc.* 60, 309 (1938).